Editors' Suggestion | Featured in Physics

Water Impact: When a Sphere Becomes Flat

Jesse Belden,[1,*] Nathan Speirs,[2] Aren Hellum,[1] George Loubimov,[1] and Tadd T. Truscott[3]
[1]Naval Undersea Warfare Center Division Newport, Newport, Rhode Island 02841, USA
[2]Brigham Young University, Provo, Utah, USA
[3]King Abdullah University of Science and Technology (KAUST), Thuwal 23955-6900, Kingdom of Saudi Arabia

(Received 13 October 2023; accepted 22 May 2024; published 16 July 2024)

A large hydrodynamic force accompanies the vertical impact of bodies on water. While added mass phenomena govern these forces for both spherical and flat impactors, the dynamics of a trapped gas layer critically alters the flat case, reducing the peak pressure below that predicted by water hammer theory. An impactor with a spherical nose cap looks increasingly flat as the nose curvature approaches zero. This causes one to ask at what curvature a spherical cap impactor transitions to flat impact behavior. We find this transition, relate limiting behaviors to theories, and dispel the long-held belief that the largest water impact forces occur for flat bodies.

DOI: 10.1103/PhysRevLett.133.034002

The vertical impacts of rigid bodies on water are characterized by impulsive slamming forces during the very early stages of water entry [1–7] (Fig. 1). The peak force magnitude is significantly larger than the ensuing steady cavity-running forces, e.g., approximately double for a sphere [8] and 2 orders of magnitude larger for a flat disk [9]. Thus, understanding these water impact forces is of importance for engineered and biological applications including, ship hull slamming [10,11], naval structure design [1,2,8], spacecraft water landing [12], diving birds [13,14], water-walking lizards [15], and injuries in human Olympic diving [16,17].

To support these various fields, basic studies have investigated impact forces on canonical geometries including spheres and flat disks. For sphere impacts, the analytical force model of Shiffman and Spencer (S&S) [18] has been confirmed by experiments for a range of sphere radii r [19–21]. The transient force is driven by added mass as a growing surface area of the sphere becomes continuously wetted and accelerates liquid from rest. On the other extreme, impact of a flat disk on flat water is a theoretically singular event that is mediated in reality by a gas layer trapped below the impactor face that deforms the water surface prior to impact [9,22–29] [Fig. 1(c)]. While added mass still governs the disk impact force, the magnitude is significantly larger than for a spherical impact. Yet, a cylinder with a spherical end cap looks increasingly flat as the nose radius $r \to \infty$, raising the question of when and how the transition occurs between spherical and flat impact behavior. Given the potential for catastrophic damage to bodies with flat surfaces, a thorough understanding in this regime is required yet has remained unresolved until now.

A study of flat and convex impactors found that the average added mass over the slamming phase was relatively insensitive to nose curvature, and matched theory for a circular flat-bottomed disk [30]. The authors reported, however, that the largest accelerations and shortest loading timescale occurred for the flat impactor, which indicates that the dynamics are more subtle than can be represented by the average added mass. Thus, the details of how and when a convex (spherical) impactor behaves as a flat disk remain elusive. In this Letter, we aim to resolve the transition in water impact behavior between flat and spherical shapes. To characterize the transition, we study the variation in impact force coefficient and trapped air layer dynamics as a function of nose radius. We challenge the assumption that the largest vertical impact force is expected for a flat-nosed impactor [30] and test the hypothesis that the largest force actually occurs for a convex impactor. Our findings are explained by two intersecting models: a modification to the S&S theory for sphere impact, and a model that considers air cushioning for nearly flat spherical cap impactors.

In order to find the sphere-flat disk transition, we experimentally measure the impact forces on a body free-falling from different drop heights into quiescent water (density ρ) to give an impact speed range of $U = 1$–4 m/s. The body has a cylindrical aluminum housing with

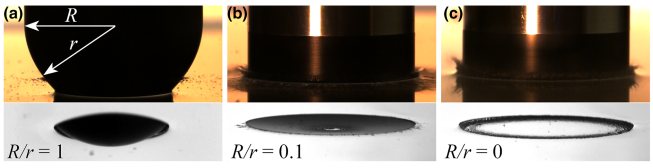

FIG. 1. Images above and below water at the moment of peak water impact force for bodies with a spherical cap nose of radii (a) $r = 22.2$ mm ($U = 1.2$ m/s), (b) $r = 222$ mm ($U = 1.4$ m/s), (c) $r = \infty$ (flat; $U = 1.4$ m/s). The cross-sectional radius of the cylindrical body is $R = 22.2$ mm.

 © 2024 American Physical Society

cross-sectional radius R that accommodates different spherical cap noses with radius r [Fig. 1(a)]. We vary the nose radius from $r = R$ to $r = \infty$ (i.e., flat), with a very fine spacing as $r \to \infty$. A three-axis accelerometer rigidly mounted inside the body directly measures acceleration a at 20 kHz. The impact force is computed as $F(t) = ma(t)$, with the body mass $m = 421$ g and the nose mass ranging from $m = 96$–159 g. We simultaneously use two high-speed cameras to visualize the event (Fig. 1) and to measure U and α, the angle between the body face and water surface at the moment of impact. We only consider cases with $\alpha \leq 0.2°$ for the flatter noses ($0 \leq R/r \leq 0.1$) [28,31] (see Supplemental Material [32], Sec. S1, for further experimental details).

We find that the force coefficient based on the body radius, $C_R = ma(t)/(0.5\rho U^2 \pi R^2)$, increases with the radius of the nose r (Fig. 2(a)). Our bodies with a hemispherical nose ($R/r = 1$) recover the sphere impact force behavior predicted by the S&S theory, peaking at $C_R = 1.07$ at a normalized submergence of $Ut/R = 0.13$, as shown in Fig. 2(a) (inset). For this nose, and for the $R/r = 0.75$ nose, the force peak occurs prior to the spherical cap being fully wetted. For $0.15 \leq R/r \leq 0.5$, C_R increases to a peak and then rapidly falls off. By correlating our high speed images with the force measurements, we observe that the force peak coincides with the moment that the spherical cap becomes fully wetted. These trends continue for $R/r = 0.05$ and 0.1, with the addition of notable oscillations in C_R during the impact period [Fig. 2(b)]. The characteristics of the impact forces are also captured by computational fluid dynamics (CFD) simulations, which show excellent agreement with the data (see Supplemental Material [32], Sec. S2, for CFD details). At $R/r = 0.008$ the force coefficient from CFD peaks at $C_R \approx 170$, 2 orders of magnitude larger than for the hemisphere and *larger* than the peak C_R for the $R/r = 0$ (flat) nose [Fig. 2(c)].

To test which noses behave as spheres, we renormalize using the nose radius, yielding $C_r = ma(t)/(0.5\rho U^2 \pi r^2)$ and Ut/r, and compare results for each nose to the S&S theory for sphere impact. If a nose behaves like a sphere we expect C_r to be predicted by the theory up to the moment the spherical cap is fully wetted, which depends on cap height h and the rise up of the water surface. Figure 2(d) shows that the experimentally measured peak values of C_r are well-captured by this modified S&S theory for all spherical cap noses except $R/r = 0.008$, for which the peak C_r is overpredicted. We observe that the $R/r = 0.008$ nose completely submerges below the quiescent free surface prior to the occurrence of the peak force. This is unlike all of the other spherical cap noses tested, which experience peak force prior to submergence of the cap below the quiescent free surface (see Supplemental Material [32], Sec. S3, for more details). Thus, we conclude that below some value of R/r (shown later to be $R/r \lessapprox 0.023$), the peak force deviates from spherelike impact behavior. We next explain the physical phenomena accompanying the transition from sphere to flat impact behavior.

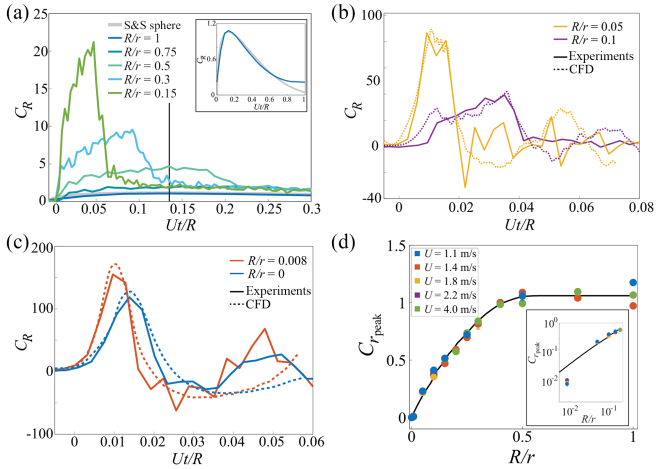

FIG. 2. (a) Impact force coefficients C_R for noses spanning the range of $R/r = 0.15$–1; $t = 0$ corresponds to the moment of first wetting of the nose. Vertical line shows location of max C_R for a sphere. Results for (b) $R/r = 0.05$ and 0.1 and (c) $R/r = 0$ and 0.008 show excellent agreement between CFD and the experimental data. All cases in (a)–(c) impact at $U = 1.4$ m/s. (d) Comparison of impact behavior to the modified sphere impact model of Shiffman and Spencer. The peak force coefficient based on nose radius $C_{r_{\text{peak}}}$ is well-predicted by the modified S&S theory (black curve) for $R/r \geq 0.05$. The inset shows the overprediction of $C_{r_{\text{peak}}}$ for $R/r = 0.008$.

The dynamics of the air layer captured between the impacting nose and the water changes with the nose radius. Figure 3 shows below-surface views of the impact for the four flattest noses. For $R/r = 0.1$ and 0.05, the first water contact occurs in a ring such that a small air pocket is trapped on the nose at impact as previously described for sphere impact [37–39]. The outer contact line of the ring then travels continuously outward wetting the spherical cap progressively. Prior studies of spherical body impact on a liquid pool [37–39], and liquid droplet impact on a flat solid surface [39–49] have shown that the radius of the initially trapped gas pocket is $r_p = 3.8(4\mu_g/\rho U)^{1/3} r^{2/3}$, where μ_g is the gas viscosity. For our impactors, we expect to reach a critical nose radius, $r = r_{\text{crit}}$, above which the gas pocket covers the face of the impactor (i.e., $r_p = R$). Setting $r_p = R$ in the above equation, we compute $R/r_{\text{crit}} = 0.013$–$0.006$ for impact speeds ranging from $U = 1$–4 m/s, respectively. Experimentally we find that an air layer indeed covers all but the periphery of the nose at impact for the $R/r = 0.008$ and 0 noses [Figs. 3(c) and 3(d)]. This phenomenon is a disklike behavior and is well-described in the literature for flat disk impact [9,22,25,27,50]. The explanation for disks is as follows. Prior to impact the gas between the nose and the water pressurizes, causing a concave depression of the liquid

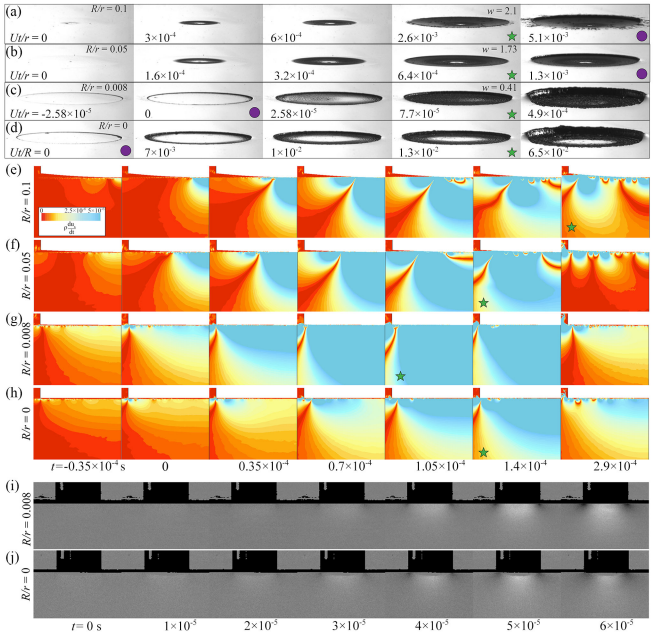

FIG. 3. Air layer and liquid response in the early moments of impact. Below-surface high speed camera views (30 000 fps) show the wetting characteristics and air entrapment for noses: (a) $R/r = 0.1$, (b) $R/r = 0.05$, (c) $R/r = 0.008$, (d) $R/r = 0$, all impacting at $U = 2.2$ m/s. The time of peak force is denoted by green stars, and the purple circles denote the time at which the cap edge submerges to the quiescent free surface. The added mass is visualized for the same nose shapes from CFD simulations at $U = 2$ m/s: (e) $R/r = 0.1$, (f) $R/r = 0.05$, (g) $R/r = 0.008$, (h) $R/r = 0$. The contours show $\rho(du_x/dt)$ (same scale applies to all images) and again the green stars denote the peak force time. The dimensional times labeled below (h) are the same for each image sequence shown in (e)–(h). Schlieren images show a local pressure rise beneath the nose for (i) $R/r = 0.008$ and (j) $R/r = 0$ at $U = 3.5$ m/s, consistent with hydrodynamic timescales. Increasing light intensity in the vertical direction indicates an increasing pressure gradient. The dimensional times labeled below (j) apply to (i), (j). The cases in (a)–(d) are shown in Supplemental Videos 1-4, and (i),(j) are shown in Supplemental Videos 5-6 [32].

surface below the disk face and a rise up of the surface below the edge. Thus, first water contact occurs near the perimeter of the nose, trapping an air layer beneath. Therefore, as $R/r \to 0$ the impacting body begins to show gas entrapping behavior that is disklike.

The details of the air cushioning layer and the concave surface depression are critical for understanding the impact forces for the flattest noses [27,29]. To shed light on the nose-air-surface interplay, we designed the $R/r = 0.008$ nose to be in the range of R/r_{crit} defined earlier. We made this choice to test two hypotheses: (1) matching the nose geometry to the deformed surface geometry should reduce the amount of air trapped relative to a flat disk, and (2) as a result, the rate of change of added fluid momentum and thus the peak impact force will be larger than for a flat disk.

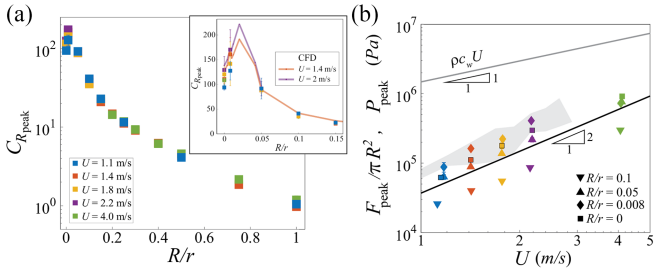

FIG. 4. Transition in impact force behavior as spherical noses become flat. (a) Peak impact force coefficient $C_{R_{\mathrm{peak}}}$ from experiments for all noses and all speeds. Inset shows enlarged view as $R/r \to 0$. CFD results for $C_{R_{\mathrm{peak}}}$ are shown for additional values of R/r. (b) Peak force from experiments normalized by πR^2 as a function of impact speed. The data follow a scaling with U^2 (black curve). The $R/r = 0$ data agree with the range of peak pressures reported in [9] (shaded gray region). The legend colors in (a) apply to the data markers in (b).

The first hypothesis is supported by our imaging [Figs. 3(c), 3(d) and Supplemental Videos 3-4], which indicates fewer and smaller air bubbles trapped beneath the $R/r = 0.008$ nose after impact. For context on the second hypothesis, we turn attention to the mechanism driving the large force peak associated with water impact.

For spheres and flat disks alike, prior experiments have shown that the impulsive impact force stems from the rate of change of the added fluid momentum [9,18]. This can be conceptualized as $d[m_a u]/dt = m_a(du/dt) + u(dm_a/dt)$, where u is the instantaneous velocity of the added mass $m_a = \rho V_a(t)$, and V_a is the volume containing the added fluid mass. For a general body, the time rate of change of both u and V_a contribute to the force. We quantify this in the vertical direction (x, aligned with U) using contours of $\rho(du_x/dt)$ from CFD [Figs. 3(e)–3(h)]. For the $R/r = 0.008$ nose the volume of liquid within a given $\rho(du_x/dt)$ contour is greater than for any other nose at each time instant. The extent and spatial growth rate of these contours show that m_a and (dm_a/dt) are larger for the $R/r = 0.008$ nose. Based on this liquid response to impact, one would expect a larger transient impact force to occur for the $R/r = 0.008$ nose as compared with the flat disk. Figures 4(a) and 4(b) show this to be the case for all impact speeds tested both experimentally and with CFD. The mean peak force for the $R/r = 0.008$ nose taken over several trials is remarkably 24%–45% larger than for the flat disk depending on speed, despite such a seemingly minor geometry difference (spherical cap height of the $R/r = 0.008$ nose is 90 μm). Additional CFD simulations show that $R/r = 0.021$ produces an even larger $C_{R_{\mathrm{peak}}}$ [Fig. 4(a) inset], indicating that the peak force for disklike noses is sensitive to the coupling between the nose shape, air layer dynamics, and free-surface deformation. We next seek to theoretically rationalize this coupling and estimate the value of R/r that maximizes impact force.

To determine how the gas layer dynamics affect the peak impact force, we idealize the trapped gas pocket as a piston

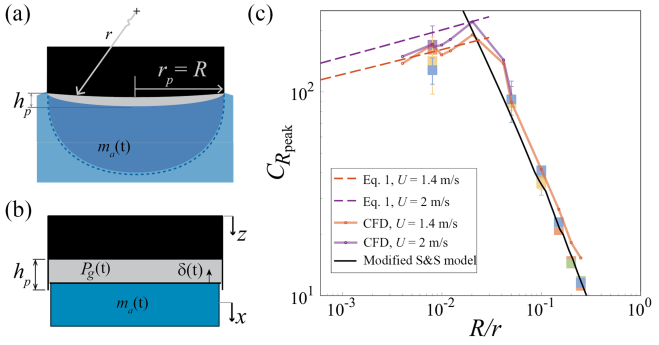

FIG. 5. (a) Schematic and (b) idealized model of a trapped gas layer covering the entire face of the impactor. (c) Predictions of $C_{R_{peak}}$ from our air-cushioned model [Eq. (1)] agree well with CFD data for $R/r \lessapprox 0.023$. Experimental data markers are the same as for Fig. 4(b).

cylinder with trapped gas layer of initial height h_p and radius R, and piston mass equal to the added mass $m_a(t)$, as shown in Figs. 5(a) and 5(b). For spherical impactors, Li and Thoroddsen [48] found that $h_p = rSt^{2/3}(4.2\epsilon^{2/5})$, where the Stokes number is $St = (\mu_g/\rho U r)$ and $\epsilon = (P_{atm}/\rho U^2)St^{1/3}$ is a compressibility factor [44,45,48,49]. The pressure in the gas layer is $P_g = P_0(1-\delta/h_p)^{-\gamma}$ [44], where δ is the time-varying displacement of the gas-liquid interface, P_0 is the initial pressure in the gas layer, and $\gamma = 1.4$ (adiabatic index of air). We can linearize P_g for small displacements about $\delta = 0$ as $P_g \approx P_0[1+\gamma(\delta/h_p)]$. The net vertical force on the impactor is $F = (P_g - P_{atm})\pi R^2$; using the above definitions for P_g and h_p, the body force coefficient can be written as

$$C_R \approx \frac{2P_0}{\rho U^2}\left(\frac{R}{r}\right)^{\frac{1}{5}}\left(\frac{\delta}{R}\right)\left[\frac{\gamma}{4.2St_R^{\frac{4}{5}}\left(\frac{P_{atm}}{\rho U^2}\right)^{\frac{2}{5}}}\right] + C_{P_0} \quad (1)$$

where $St_R = (\mu_g/\rho U R)$ and $C_{P_0} = (P_0 - P_{atm})/\frac{1}{2}\rho U^2$. Equation (1) predicts $C_{R_{peak}}$ at the max compression $\delta = \delta_{peak}$, given expressions for P_0 and δ_{peak}. From prior work [44,45], the initial pressure $P_0 = \rho U^2\sqrt{R/h_p} + P_{atm}$. A scaling analysis of the balance of forces on the added mass yields

$$\frac{\delta_{peak}}{R} = \frac{4\rho U h_p}{3\pi\gamma P_0 \tau} - \frac{h_p}{\gamma R}\left(1 - \frac{P_{atm}}{P_0}\right). \quad (2)$$

Here, the timescale τ is estimated from the natural period of our idealized system such that $\tau = 2\pi\sqrt{\kappa m_{a_p}/k}$, where $k = \pi R^2 P_0(\gamma/h_p)$ is a spring constant, m_{a_p} the peak added mass, and $0 < \kappa < 1$ is a constant accounting for the fact that the added mass varies over the impact event. Equation (2) along with the expressions for τ, P_0, and h_p can be inserted into Eq. (1) to predict $C_{R_{peak}}$ with only one fitting parameter κ (see Supplemental Material [32], Sec. S4, for complete model details).

Figure 5(c) plots the curves resulting from Eq. (1) evaluated at $U = 1.4$ and 2 m/s with $\kappa = 0.45$. Our idealized model agrees well with the CFD results for $R/r \lessapprox 0.023$, capturing the dependence of $C_{R_{peak}}$ on R/r and U. The model curves intersect the modified S&S model at $R/r = 0.023$ ($U = 1.4$ m/s) and 0.019 ($U = 2$ m/s), which are in excellent agreement with $R/r = 0.021$, where CFD predicts the maximum $C_{R_{peak}}$. Note that these values of r yielding the maximum peak impact force are smaller than r_{crit} and correspond to $r_p/R \approx 0.6$. Thus, the mediating effect of the gas layer occurs prior to the impactor face being fully covered by the gas layer. The air cushioning effect grows (i.e., reduces $C_{R_{peak}}$) as $R/r \to 0$, first through an increase in both the gas pocket height h_p and radius r_p, and then only through h_p once $r_p = R$.

The above describes a hydrodynamic phenomenon driving the peak force. The literature has theorized that in the absence of an air layer, the limiting pressure on a flat impactor is the acoustic water hammer pressure, scaling as $P_{peak} \sim \rho c_w U$ with c_w the speed of sound in water [22,25,51–53]. In the presence of an air layer, prior experiments showed the peak pressure to be much smaller than $\rho c_w U$ and found $P_{peak} \propto U^2$, indicating that hydrodynamic effects dominate the impact forcing [8,9,22,51,53]. We find that our measurements of $P_{peak} = F_{peak}/\pi R^2$ (i.e., peak average pressure) are in agreement with the direct peak pressure measurements from [9] for flat disks [shaded region in Fig. 4(b)], are all well below the water hammer pressure, and all follow the scaling $P_{peak} \propto U^2$.

Schlieren imaging lends further support for a dominant hydrodynamic forcing mechanism for our disklike impactors. Figures 3(i) and 3(j) ($R/r = 0.008$ and 0) show a smooth pressure rise beneath the nose, revealed by vertical variations in light intensity, which indicate pressure gradients. These observations match the behavior of pressure and added mass contours computed from CFD (shown in Supplemental Material [32], Sec. S5). Therefore, prior work along with our experimental and computational evidence supports the following interpretation. Prior to and just after impact, the advancing nose pressurizes the air layer and this pressure increase gets communicated to the liquid without evidence of discontinuous pressure jumps (i.e., shock waves). The pressure rises in the liquid over a timescale consistent with hydrodynamic added mass effects. The peak pressure on the nose is thus dominated by added mass.

We have revealed the transition between spherical and flat disk water impact. The impact forces on spherical impactors are well-described by the Shiffman and Spencer theory down to $R/r \approx 0.023$. For $R/r \lessapprox 0.023$, the trapped

air layer between the nose and the deformed water surface plays a significant role in the impact process. Surprisingly, we find that the maximum impact force coefficient $C_{R_{\text{peak}}}$ occurs not for a flat disk, but instead for a slightly convex nose that traps a thinner air layer and induces a larger peak rate of change of added fluid momentum. The thicker air layer generated by the flat disk impact reduces the force peak and elongates the duration of impact, but the resulting impulse over the impact period was found to be comparable to the $R/r = 0.008$ nose (see Supplemental Material [32], Sec. S5). Thus, an approach of computing the change in body momentum over the impact would result in the same average added mass value for these two noses; however, the transient force is quite different in both time and amplitude.

Our study reveals the subtle yet important variation in water impact dynamics as nose geometry becomes flat. The peak force coefficient for a nearly flat body exceeds that for most canonical nose shapes so significantly (*2 orders of magnitude* compared to a sphere) that applications should consider this extreme possibility, even if it occurs over a narrow range of conditions. We find that this narrow regime is governed by the dynamics of a trapped air layer that also has a rich history in the droplet impact literature [38–49]. We expect our results to inform a range of engineered [1,2,8,10–12] and biological [13–17] systems of the dramatic impact force when a nearly flat body enters water.

J. B., A. M. H. and G. L. acknowledge funding from the Naval Undersea Warfare Center In-House Laboratory Independent Research program, monitored by Dr. Elizabeth Magliula. T. T. T. acknowledges funding from the Office of Naval Research, Navy Undersea Research Program (Grant No. N0001414WX00811), monitored by Ms. Maria Medeiros.

*Corresponding author: jesse.l.belden2.civ@us.navy.mil

[1] T. Von Karman, The impact on seaplane floats during landing, National Advisory Committee on Aeronautics, Technical Report No. 321, 1929.
[2] H. Wagner, ZAMM-J. Appl. Math. Mech./Z. Angew. Math. Mech. **12**, 193 (1932).
[3] A. Korobkin and V. Pukhnachov, Annu. Rev. Fluid Mech. **20**, 159 (1988).
[4] R. Zhao and O. Faltinsen, J. Fluid Mech. **246**, 593 (1993).
[5] A. Korobkin, Eur. J. Appl. Math. **15**, 821 (2004).
[6] T. T. Truscott, B. P. Epps, and J. Belden, Annu. Rev. Fluid Mech. **46**, 355 (2014).
[7] U. Jain, V. Novaković, H. Bogaert, and D. Van Der Meer, J. Fluid Mech. **934**, A27 (2022).
[8] A. May, Water entry and the cavity-running behavior of missiles, Navsea Hydroballistics Advisory Committee Silver Spring Md Technical Report No. SEAHAC/TR 75-2, 1975.
[9] U. Jain, P. Vega-Martínez, and D. Van Der Meer, J. Fluid Mech. **928**, A31 (2021).
[10] G. Kapsenberg, Phil. Trans. R. Soc. A **369**, 2892 (2011).
[11] O. M. Faltinsen, J. Marine Sci. Technol. **5**, 49 (2000).
[12] C. Seddon and M. Moatamedi, Int. J. Impact Eng. **32**, 1045 (2006).
[13] B. Chang, M. Croson, L. Straker, S. Gart, C. Dove, J. Gerwin, and S. Jung, Proc. Natl. Acad. Sci. U.S.A. **113**, 12006 (2016).
[14] L. Vincent, T. Xiao, D. Yohann, S. Jung, and E. Kanso, J. Fluid Mech. **846**, 508 (2018).
[15] S. T. Hsieh and G. V. Lauder, Proc. Natl. Acad. Sci. U.S.A. **101**, 16784 (2004).
[16] B. D. Rubin, Clin. Sports Med. **18**, 293 (1999).
[17] S. M. Harrison, R. C. Cohen, P. W. Cleary, S. Barris, and G. Rose, in *Ninth International Conference on CFD in the Minerals and Process Industries* (CSIRO, Melbourne, 2012), pp. 10–12.
[18] N. Shiffman and D. Spencer, The force of impact on a sphere striking a water surface, Technical Report No. AMG-NYU-133, New York University, NY, Courant Inst of Mathematical Sciences, 1945.
[19] M. Moghisi and P. T. Squire, J. Fluid Mech. **108**, 133 (1981).
[20] N. B. Speirs, J. Belden, Z. Pan, S. Holekamp, G. Badlissi, M. Jones, and T. T. Truscott, J. Fluid Mech. **863**, 956 (2019).
[21] J. T. Antolik, J. L. Belden, N. B. Speirs, and D. M. Harris, J. Fluid Mech. **974**, A23 (2023).
[22] S.-L. Chuang, J. Ship Res. **10**, 10 (1966).
[23] S. Howison, J. Ockendon, and S. Wilson, J. Fluid Mech. **222**, 215 (1991).
[24] S. Okada and Y. Sumi, J. Marine Sci. Technol. **5**, 31 (2000).
[25] E. Ermanyuk and M. Ohkusu, J. Fluids Struct. **20**, 345 (2005).
[26] M. R. Moore, J. Eng. Math. **129**, 6 (2021).
[27] U. Jain, A. Gauthier, D. Lohse, and D. van der Meer, Phys. Rev. Fluids **6**, L042001 (2021).
[28] N. B. Speirs, K. R. Langley, Z. Pan, T. T. Truscott, and S. T. Thoroddsen, Nat. Commun. **12**, 7250 (2021).
[29] Y. L. Fan, U. Jain, and D. van der Meer, Phys. Rev. Fluids **9**, 010501 (2024).
[30] E. Ermanyuk and N. Gavrilov, J. Appl. Mech. Tech. Phys. **52**, 889 (2011).
[31] J. Belden, N. B. Speirs, A. M. Hellum, M. Jones, A. J. Paolero, and T. T. Truscott, J. Fluid Mech. **963**, A14 (2023).
[32] See Supplemental Material at http://link.aps.org/supplemental/10.1103/PhysRevLett.133.034002, which includes Refs. [33–36], for additional information about the experimental methods, computational method, and analytical modeling.
[33] C. W. Hirt and B. D. Nichols, J. Comput. Phys. **39**, 201 (1981).
[34] M. Darwish and F. Moukalled, Numer. Heat Transfer **49**, 19 (2006).
[35] D. Jang, R. Jetli, and S. Acharya, Numer. Heat Transfer **10**, 209 (1986).
[36] G. S. Settles and M. J. Hargather, Meas. Sci. Technol. **28**, 042001 (2017).
[37] J. Marston, J. Fluid Mech. **680**, 660 (2011).

[38] P. Hicks, E. Ermanyuk, N. Gavrilov, and R. Purvis, J. Fluid Mech. **695**, 310 (2012).
[39] P. D. Hicks and R. Purvis, J. Fluid Mech. **735**, 120 (2013).
[40] F. Smith, L. Li, and G. Wu, J. Fluid Mech. **482**, 291 (2003).
[41] A.-L. Biance, C. Clanet, and D. Quéré, Phys. Rev. E **69**, 016301 (2004).
[42] S. Thoroddsen, T. Etoh, K. Takehara, N. Ootsuka, and Y. Hatsuki, J. Fluid Mech. **545**, 203 (2005).
[43] A. Korobkin, A. Ellis, and F. Smith, J. Fluid Mech. **611**, 365 (2008).
[44] S. Mandre, M. Mani, and M. P. Brenner, Phys. Rev. Lett. **102**, 134502 (2009).
[45] M. Mani, S. Mandre, and M. P. Brenner, J. Fluid Mech. **647**, 163 (2010).
[46] P. D. Hicks and R. Purvis, J. Fluid Mech. **649**, 135 (2010).
[47] Y. Liu, P. Tan, and L. Xu, J. Fluid Mech. **716**, R9 (2013).
[48] E. Li and S. T. Thoroddsen, J. Fluid Mech. **780**, 636 (2015).
[49] C. Josserand and S. T. Thoroddsen, Annu. Rev. Fluid Mech. **48**, 365 (2016).
[50] I. R. Peters, D. van der Meer, and J. M. Gordillo, J. Fluid Mech. **724**, 553 (2013).
[51] A. Korobkin, in *Proceedings of the 10th Workshop on Water Waves and Floating Bodies, Oxford, UK, Apr* (iwwwfb.org, Oxford, 1995), pp. 2–5, http://www.iwwwfb.org/Workshops/10.htm.
[52] M. M. Daou, E. Igualada, H. Dutilleul, J.-M. Citerne, J. Rodríguez-Rodríguez, S. Zaleski, and D. Fuster, AIChE J. **63**, 2483 (2017).
[53] S. S. Cook, Proc. R. Soc. A **119**, 481 (1928).